



Failure analysis of electrolyte-supported solid oxide fuel cells



Felix Fleischhauer ^{a,b,*}, Andreas Tiefenauer ^c, Thomas Graule ^a, Robert Danzer ^b, Andreas Mai ^d, Jakob Kuebler ^a

^a Empa, Swiss Federal Laboratories for Materials Science and Technology, Laboratory for High Performance Ceramics, Ueberlandstr. 129, 8600 Duebendorf, Switzerland

^b Institut für Struktur-und Funktionskeramik, Montanuniversität Leoben, Peter-Tunner-Str. 5, 8700 Leoben, Austria

^c ZHAW Zürich University of Applied Sciences, Institute of Computational Physics, 8401 Winterthur, Switzerland

^d Hexis Ltd., Zum Park 5, 8404 Winterthur, Switzerland

HIGHLIGHTS

- Failure analysis of SOFCs run under realistic operating conditions.
- Modelling of present stresses acting on the cell.
- Measurement of the residual stresses.
- Strength of the 3YSZ- and 6ScSZ-electrolytes.
- Failing mechanism of the cells has been elucidated.

ARTICLE INFO

Article history:

Received 12 August 2013

Received in revised form

7 January 2014

Accepted 4 February 2014

Available online 21 February 2014

Keywords:

Fuel cells

Mechanical failure

Failure analysis

Residual stress

Mechanical strength

Thermal stress

ABSTRACT

For solid oxide fuel cells (SOFCs) one key aspect is the structural integrity of the cell and hence its thermo mechanical long term behaviour. The present study investigates the failure mechanisms and the actual causes for fracture of electrolyte supported SOFCs which were run using the current μ -CHP system of Hexis AG, Winterthur – Switzerland under lab conditions or at customer sites for up to 40,000 h.

In a first step several operated stacks were demounted for post-mortem inspection, followed by a fractographic evaluation of the failed cells. The respective findings are then set into a larger picture including an analysis of the present stresses acting on the cell like thermal and residual stresses and the measurements regarding the temperature dependent electrolyte strength.

For all investigated stacks, the mechanical failure of individual cells can be attributed to locally acting bending loads, which rise due to an inhomogeneous and uneven contact between the metallic interconnect and the cell.

© 2014 Elsevier B.V. All rights reserved.

1. Introduction

1.1. Background

Solid Oxide Fuel Cell (SOFC)-based systems are promising candidates for the conversion of chemical energy stored in natural gas

or hydrogen into electricity. Due to the direct electro-chemical process it is possible to reach electrical efficiencies of 70% and more. Therefore, a lot of effort has been undertaken to develop systems which provide these high efficiencies while using materials and processing routes which are commercially acceptable. After several decades of intensive fundamental and materials research some systems are on the market (for instance the *BlueGen* of *CFCL* and *Bloom's Energy Server* of *Bloom Energy*) or are close to their introduction (e.g. the *Galileo 1000 N* of *Hexis*). But despite the progress which is reflected in the availability of these devices nowadays, there is still room for improvement. Especially the long term issues have gotten more and more in the focus of the respective manufacturers. Some of the main problems which need to be improved are anode degradation, oxidation of the metallic

* Corresponding author. Empa, Swiss Federal Laboratories for Materials Science and Technology, Laboratory for High Performance Ceramics, Ueberlandstr. 129, 8600 Duebendorf, Switzerland.

E-mail addresses: Felix.Fleischhauer@empa.ch (F. Fleischhauer), Andreas.Tiefenauer@sensirion.com (A. Tiefenauer), Thomas.Graule@empa.ch (T. Graule), isfk@unileoben.ac.at (R. Danzer), Andreas.Mai@hexis.com (A. Mai), Jakob.Kuebler@empa.ch (J. Kuebler).

interconnects, chromium poisoning of the cathode and the long-term thermo mechanical stability of the whole cell and that within the frame of real operation conditions, like multiple thermo and redox cycles, variation in the quality of gas composition and accidental exposure to sulphur [1–4].

In this study the fracture behaviour and the individual causes for cell fracture of electrolyte supported fuel cells under real operational conditions are investigated. The examined cells were provided by Hexis AG in Switzerland and run in the company's current SOFC-System, the GALILEO 1000 N.

One of the main tasks of the electrolyte is to physically separate the fuel from its oxidant, which it fails after its fracture. In any case the resulting intra cellular leakage will have a short- or long-term impact on the overall stack performance and could in the worst case lead to the instantaneous death of the respective fuel cell system [5].

Some experimental works have already been published regarding the mechanical stability of electrolyte supported cells [6–8] and the fracture behaviour outside a system at ambient conditions [9,10], but so far none to our knowledge where cell fracture has been considered and investigated within the environment of an actual operating system.

1.2. System and stack

The Galileo 1000 N employs a stack with a planar open radial design as sketched in Fig. 1. Since the stack is “open”, cells are required to maintain their structural integrity upon multiple redox-cycling. Currently, only electrolyte supported cells are able to fulfil this demand while having the drawback of a higher ohmic resistance compared to anode supported cells. On the other hand the open design allows the stack mounting to be a relative simple process. The nominal operation temperature is 850 °C, measured at the bottom metallic interconnect MIC. The fuel is supplied after being partially catalytically oxidized through the centre hole of the stack onto the cell via the inner gas inlet channels of the anode side of the MIC (see Fig. 1). A fuel sealing plane at the opposite side

prevents leakage onto the cathode. The air streams from the outside along four inlet channels towards the centre. It then flows back through the flowfield to the outer edge, where the non-utilised fuel is burned off and produces additional heat.

The MIC is a CrFe5 alloy manufactured and delivered by Plansee SE (Reutte, Austria) with a thermal expansion coefficient which matches that of the cell. The zirconia-electrolyte is purchased from Nippon Shokubai (Tokyo, Japan) and contained either 3 mol% of Y_2O_3 (3YSZ) or 6 mol% Sc_2O_3 (6ScSZ). These compositions were chosen due to their superior mechanical strength compared to the common electrolytes with 10 mol% Sc_2O_3 (10Sc1CeSZ) or 8 mol% Y_2O_3 (8YSZ) according to the supplier's data sheet. The discs are screen-printed with a $La_{0.75}Sr_{0.2}MnO_{3-\delta}$ (LSM)-8YSZ-cathode and a Ni–Ce_{0.4}Gd_{0.6}O_{2- δ} -anode developed by Hexis.

In order to understand the mechanisms which are responsible for cell fracture, stacks with a different operational history but the same design were chosen for post mortem inspection and fractography. Results from visual, light- and electron-microscopic analysis are then considered in a comprehensive context, laying the focus in particular on the mechanical behaviour of the electrolyte, as the element providing the cells integrity.

2. Failure analysis

2.1. Post mortem inspection and fractography

Three stacks with 3YSZ and six stacks with 6ScSZ electrolytes were taken for post mortem inspection. Each system was running either at Hexis or at customer sites under real operational conditions in the frame of the German CALLUX project [11]. The operation time ranges from 300 up to 40,000 h, the count of complete redox-cycles a stack had undergone from one to fourteen. After demounting, all examined stacks contained ruptured cells, while showing no severe or discontinuous loss in the overall performance during operation. This already indicates that the present stack design is relatively tolerant towards fracture and the resulting intra cellular leakage. This is due to the small pressure difference which is immanent to the open radial co-flow design. Nonetheless, a certain degree of leakage will happen reducing effectively the provided fuel. The quantitative assessment of the influence, which cell fracture has on the performance is the topic of a subsequent study.

The fracture pattern consists predominantly of radial cracks which can be accompanied by secondary fracture around the central hole, as seen in Fig. 3. Less often occurred cracks with a

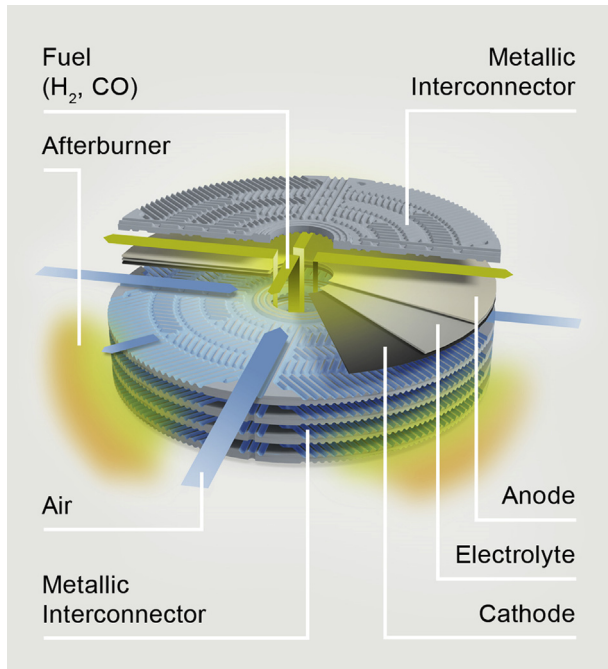


Fig. 1. Working principle of the stack of the Galileo 1000 N (courtesy of Hexis AG).

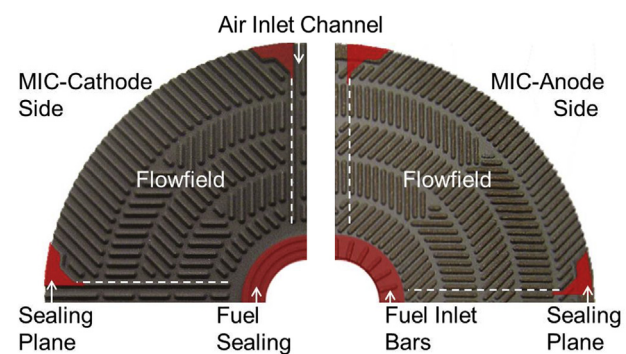


Fig. 2. Cathode side (left) and anode side (right) MIC structure with the positions of the air inlet channels and the flow-fields. The areas where frequent cell fracture is initiated are marked red. (For interpretation of the references to colour in this figure legend, the reader is referred to the web version of this article.)

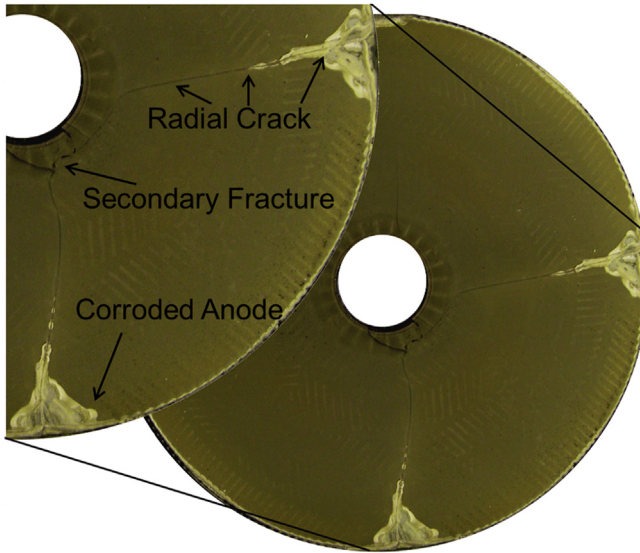


Fig. 3. Anode side of a ruptured cell after 6700 h operation and two redox-cycles.

tangential orientation, which usually followed the gaps between the bar arrays of the anode flowfield structure until at some point turning sideways, running towards the outer edge of the cell. For the stacks operated for more than 4000 h the leakage around some cracks might have caused structural changes in the anode which can be attributed to the local burning of the fuel leading to increased temperatures and concentration of water and oxygen which may oxidise the Nickel. This effect is usually more pronounced close to the outer circumference (increased water concentration due to the fuel utilised) especially above the air inlet channels where the maximum leakage rate is expected (see Fig. 3).

Fractography reveals that the majority of the cracks originate at distinct sites with respect to the MIC. These are the sealing planes on the cathode side at the air entrance and the area close to the central hole with the fuel inlet bars and the opposite fuel sealing plane (marked red in Fig. 2). At the air inlet sealing planes, fracture always is associated with small bumps of the MIC coating on the cathode side (Fig. 4(a)) with a height typically between 10 and 60 μm compared to their direct surrounding. This leads to an uneven distribution of the mechanical pre-load and the stacks own weight (which reaches up to a quarter of the pre-load). These bumps can occur randomly distributed over the whole MIC-structure. However, they coincide with fracture origin sites almost exclusively at the red marked areas in Fig. 2.

For stacks operated more than 4000 h, cracks around the central hole become more frequent without being associated with bumps of the contact coating at the fuel sealing plane of the cathode side. Since no additional seal prevents the cathode from being exposed to the fuel flowing in the central hole, it will gradually be decomposed and lose its structural integrity, becoming a loose powder not able to support the cell at the fuel sealing plane, also leading to an undefined uneven distribution of the pre-load.

Just behind the inner sealing ring the leaked fuel burns off with the cathode air, which creates a narrow zone of 0.5–0.6 mm where the decomposed cathode reacts with the electrolyte forming a new porous layer leaving the electrolyte grooved (Fig. 5). EDX indicates the formation of several different zirconate compounds like La_2ZrO_7 or SrZrO_3 , which have been already observed for LSM based cathodes [12,13]. Although the surface profile is significantly changed these grooves do not appear to be origins for fracture, but only preferential pathways for crack propagation.

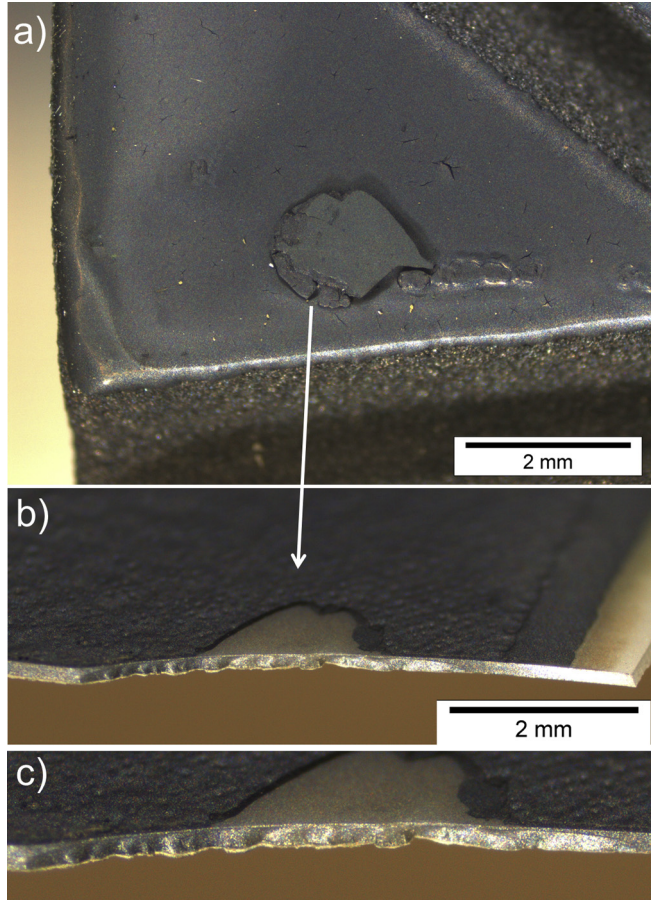


Fig. 4. Crack origin at the cathode sealing plane at the air inlet channel with (a) the associated bumps on the cathode side, (b) the fracture surface of the cell from a tilted cathode side perspective with the delaminated cathode in the contact zone and (c) the magnification of the fracture surface.

In general the crack initiation sites exhibit always the same morphology as represented by Fig. 4(b) and (c), showing a rough and jagged fracture surface which is between 2 and 4 mm wide for radial cracks and can reach up to several centimetres for cracks starting with a tangential orientation. The fracture edge at the cathode side of the electrolyte is smooth, while the anode side shows rather a zigzag pattern. The ends of these zones are marked by an edge curved concavely towards the anode (Fig. 4(c)), indicating that the crack extension did not proceed continuously but stopped, while changing the crack surface morphology after resuming propagation.

2.2. Mechanical load situation

(i) **Pre-load:** After being able to identify the location for crack initiation the question of the fracture mechanism and the involved stresses leading to macroscopic cell rupture arises. The most apparent source for mechanical stress acting on the cell is the pre-load of 390 N on the stack which results in a vertical average compression of $\sigma_{\text{prel}} = 0.036\text{--}0.046 \text{ MPa}$ considering the stacks own weight and assuming an even distribution. While these loads are very small, they might lead to significant stresses when distributed unevenly over the cell area. This is the case for the observed bumps on the cathode side which are associated with the crack origin sites. Here the pre-load is concentrated and a certain deflection, which is the height of the bumps, is impressed in the

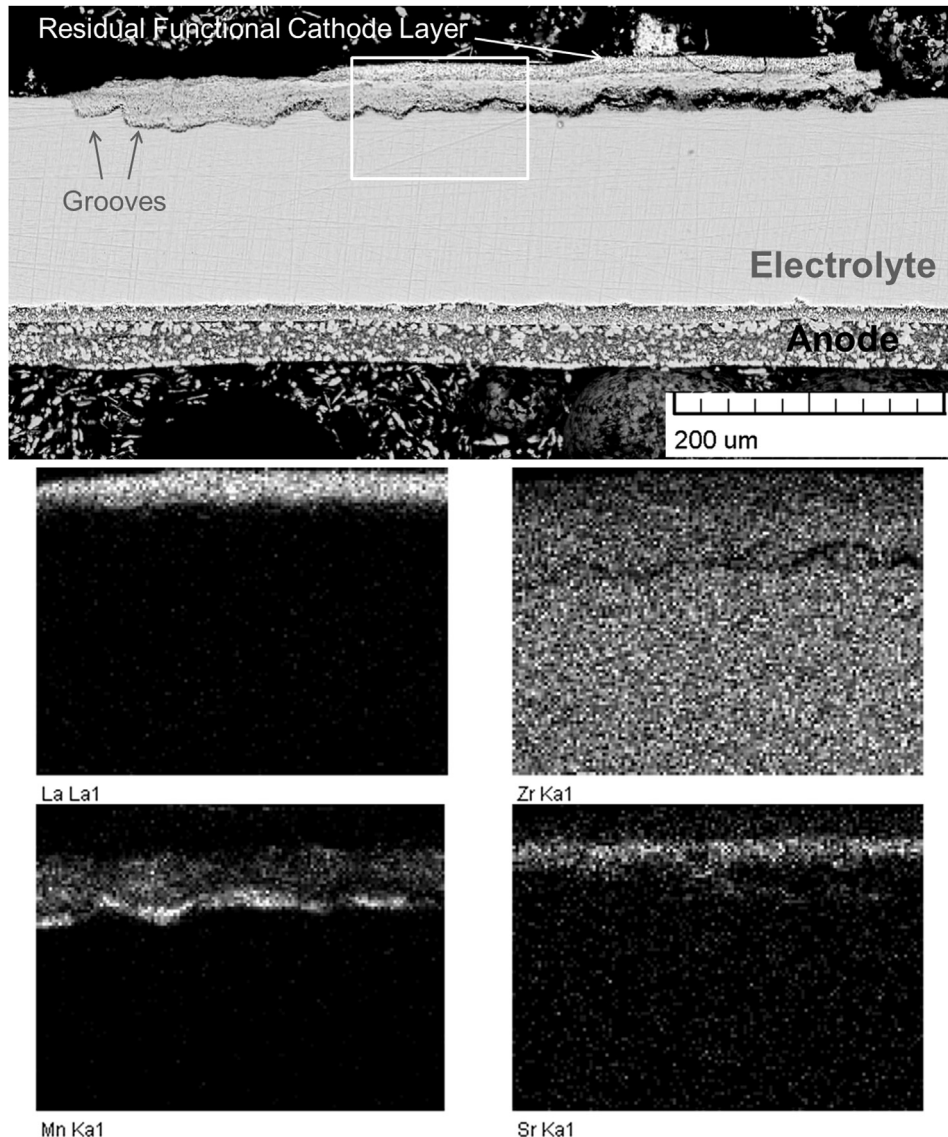


Fig. 5. Electrolyte and cathode material reactions after 40,000 h of operation. For the marked section the EDX-element mappings of La, Zr, Mn and Sr are shown (30 kV acceleration voltage).

cell. Assuming the cell to be clamped between two MICs and being lifted and pressed into the Nickel mesh the resultant stresses can be estimated. The respective elastic model is taken from *Roark's Formulas for Stress and Strain* [14] and shown in Fig. 6. This approach is just a rough image of the real load situation but can provide an upper limit of the occurring stresses, neglecting the stiffness of the Nickel mesh and a redistribution of the nominal pre-load. Since the maximum deflection y_{\max} is given by the height of the bumps, it is

possible to calculate the radius a for the lifted cell area. Taking the force W needed to bend the cell until the given deflection and comparing it with the nominal compressive stress the system provides ($W = \sigma_{\text{prel}} \pi a^2$), a becomes:

$$a = \left(\frac{16D^* y_{\max}}{\sigma_{\text{prel}}} \right)^{1/4} \quad (1)$$

where D^* is the effective plate constant at the operation temperature calculated according to Hsueh and Luttrell [15] using the values in Table 1 and assuming a Poisson's ratio of $\nu = 0.3$ for all layers. The resulting maximum stress which arises in this situation for the electrolyte at its interface with the anode is plotted for varying y_{\max} in Fig. 7 also following the approach of Hsueh and Luttrell, with:

$$\sigma(y_{\max}) = \frac{E_{\text{EI}}(t_{C_1} + t_{C_2} + t_{\text{EI}} - z_n^*)}{4\pi(1 - \nu^2)D^*} W(1 + \nu) \ln \frac{a}{r_0} \quad (2)$$

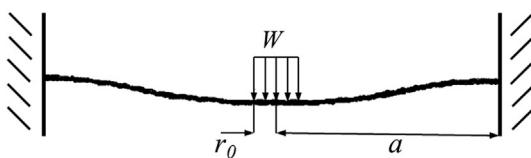


Fig. 6. Elastic model for a circular plate being fixed at the outer edge at a radius a and loaded with W evenly distributed over a radius r_0 .

Table 1

Layer thicknesses and Young's modulus for the different cell materials.

	Cathode current collecting layer	Cathode functional layer	Anode current collecting layer	Anode functional layer	3YSZ-electrolyte	6ScSZ-electrolyte
Thickness (μm)	70	15	30	10	140	160
Young's-modulus (GPa) at $T = 950\text{ }^{\circ}\text{C}$	60 ^a	40 ^a	40 ^a	60 ^a	155 ^a	140
Young's-modulus (GPa) at RT	70 ^a	80 ^a	50 ^a	65 ^a	212	202
α (25–1000 °C) ($\times 10^{-6}/\text{K}$)	11.00 ^a	10.70 ^a	12.50 ^a	12.25 ^a	10.90 ^b	10.70 ^b
ΔT after sintering (K)	1075	1075	1195	1195	—	—

^a Taken from Kuebler et al. [17].^b Values according to the supplier.

where z_n^* is the neutral bending plane of the multi-layer, E_{EI} the electrolyte's Young's modulus and t_i the respective thickness of the two cathode layers and the electrolyte and r_0 the contact radius. In order to assess the severity of these stresses the probability of failure is plotted as well using the Weibull equation [16]:

$$F(\sigma(y_{\text{max}}), S_{\text{eff}}) = 1 - \exp\left[-\frac{S_{\text{eff}}}{S_0}\left(\frac{\sigma(y_{\text{max}})}{\sigma_0}\right)^m\right] \quad (3)$$

and the material parameters given in Table 2. Since no fitting material data is available in the literature, double ring bending tests have been performed on samples 30 mm in diameter of bare 3YSZ and 6ScSZ electrolytes using the test rig and FE-model described in

Ref. [17] for evaluating the stresses and effectively loaded surfaces S_0 . Both sides of the electrolyte have been tested regarding their fracture stress at room temperature (RT) and a relative humidity of 37%, with a load rate so that the fracture time was between $t_f = 10$ –15 s, showing that the side used for the anode layers is significantly weaker, since it is rougher than the cathode side. Since the roughness apparently determines the strength, the effectively loaded surface has to be taken into account rather than the effectively loaded sample volume. The rougher side of the 6ScSZ electrolyte has also been tested at elevated temperatures giving the Young's modulus and the fracture strength values in Tables 1 and 2. Applying the values valid for $T = 950\text{ }^{\circ}\text{C}$ for the operation temperature $T \approx 850\text{ }^{\circ}\text{C}$ makes the estimation more conservative regarding the failure prediction, since the strength would rise by lowering the temperature.

It becomes apparent that the estimated stresses will most certainly not lead to fracture. Only at elevated temperatures and relatively high deflections does 6ScSZ become slightly susceptible to fracture, however bumps higher than 60 μm are scarce and thus play a lesser role. At RT the plate stiffness increases. Since the deflection is constant this leads to an increased stress, which is overcompensated by an increase in strength diminishing the likelihood for failure to be always close to zero. Because the stress is local and deformation controlled, a possible fracture event would only lead to a local crack, since any crack extension would reduce its own driving force by giving the cell the chance to comply.

(ii) *Thermal stress*: During operation the conversion rate of the fuel and therefore the released heat decreases over the cell radius leading to an inhomogeneous lateral temperature distribution. A two-step numerical simulation of the repeat unit based on the model shown in Fig. 8(a) for a cell with 3YSZ electrolyte and the layer thicknesses of Table 1 has been performed employing the finite element software NM-SESES (ZHAW-ICP, Winterthur/Switzerland). First the temperature distribution for maximum power output (MPO) and open circuit (OC) conditions over the cell is calculated employing the numerical volume averaging method [18]. The condition, where the greatest power output is reached, represents the normal operating condition for the cell. When the stack is shut down the electrical circuit is opened before the fuel is turned off, leading for a short time to a new stationary temperature distribution represented by the OC-condition. In a second step the resulting thermal stresses are calculated linear elastically using the parameters in Table 1. The resulting maximum principle stresses within the electrolyte are shown in Fig. 8(b) and (c). For the MPO-condition the electrolyte is at the outer circumference under tangential stress and slightly tangentially compressed at the inner cell area. Since the main part of the fuel is electrochemically converted at the inner cell area the temperature drops from the inside to the outside. In the case of an open circuit the whole fuel is burned off at the outer cell edge. Hence, the heat production takes place mainly at the outer edge of the cell creating a temperature gradient falling from the outside to the inside, resulting in a

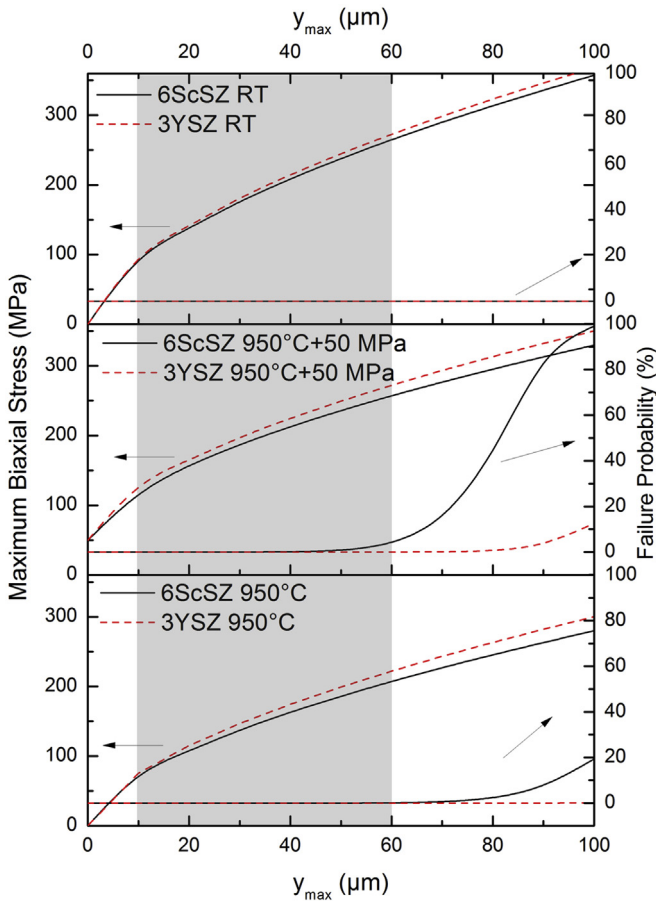


Fig. 7. Maximum biaxial stress according to the elastic model shown in Fig. 6 for a varying deflection y_{max} , $\sigma_{\text{prel}} = 0.04\text{ MPa}$, $S_{\text{eff}} = \pi r_0^2$, $r_0 = 1\text{ mm}$ and with the respective failure probability for 3YSZ and 6ScSZ electrolytes. Bottom: for $T = 950\text{ }^{\circ}\text{C}$, middle: for $T = 950\text{ }^{\circ}\text{C}$ adding 50 MPa to account for possible thermal stresses (see Fig. 8), top: for room temperature; the shaded area marks the typical height of the bumps on the cathode side.

Table 2

Electrolyte Weibull parameters for the two different electrolyte materials.

	Characteristic strength σ_0 (MPa) $T = 950^\circ\text{C}$	Characteristic strength σ_0 (MPa) $T = 25^\circ\text{C}$	Weibull modulus m	Effective surface S_0 at $T = 950^\circ\text{C}$ (mm^2)	Effective surface S_0 at $T = 25^\circ\text{C}$ (mm^2)
3YSZ	350 ^a	937	31	6.0	6.0
6ScSZ	250	701	19	14.5	11.3

^a Estimated using the relation $\sigma_0(25^\circ\text{C})/\sigma_0(950^\circ\text{C}) \approx K_{Ic}(25^\circ\text{C})/K_{Ic}(950^\circ\text{C})$ (with $K_{Ic}(T)$ being the mode I fracture toughness taken from [17]).

maximum stress which is of a tangential nature for the whole cell but also giving a positive radial component. For both conditions the peak mechanical loads are around 50 MPa appearing at the air

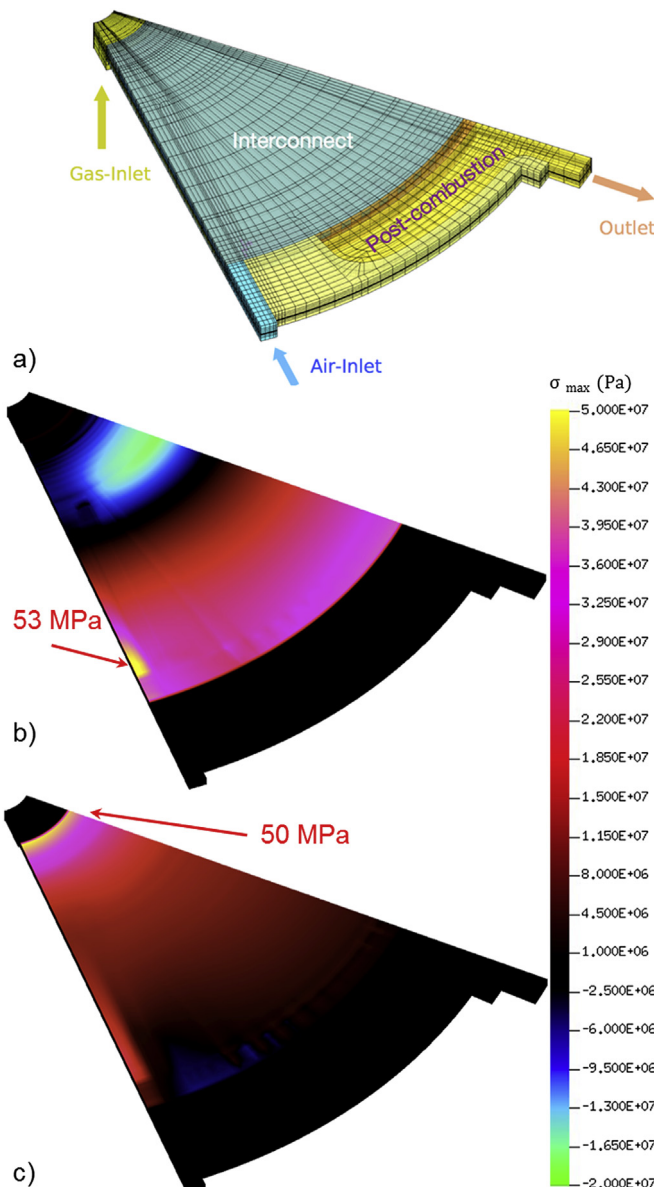


Fig. 8. (a) 3D thermo-mechanical-flow-model of 1/8th of the cell to obtain the temperature distribution within a single repeat-unit and to calculate the stresses caused by local temperature-gradients; (b) maximum principal stresses of a cell mounted in a repeat-unit under MPO-conditions and (c) under OC-conditions for a cell with 3YSZ electrolyte. The highest stresses are indicated in yellow, stress-free zones are shown in black and compressive stresses in blue and green. (For interpretation of the references to colour in this figure legend, the reader is referred to the web version of this article.)

entrance and at the inner cell edge in the case of MPO and OC respectively.

It is possible to evaluate the failure potential of thermal stresses by calculating the mode I stress intensity factor K_I for a crack being introduced at either the inner or the outer edge of the electrolyte. Following the approach proposed by Munz and Fett [19], which was already applied to a similar problem by Schneider and Danzer [20], K_I is obtained by solving:

$$K_I = \int_0^a \sigma_\phi(x) h(a, x) dx \quad (4)$$

where $h(a, x)$ is the weight function weighing the stress perpendicular to the crack faces σ_ϕ along the crack length. The respective expression for an annular circular plate can be found in the table book of Wu and Carlsson [21] and reads:

$$h(x, a) = \frac{1}{\sqrt{2\pi a}} \sum_{i=1}^{n=3,4} \beta_i(a) \left(1 - \frac{x}{a}\right)^{i-3/2} \quad (5)$$

For internal cracks n becomes 3 and for external 4. The coefficients β_i are given in Ref. [21] for discrete values of crack length a to plate width W . Fig. 9 presents the stress intensity factor solutions for an internal crack (inner edge) in the middle of the flowfield (45°) for the open circuit operation and for external cracks being introduced either in the air inlet channel (0°) or in the middle of the flowfield (45°) for MPO.

Taking the toughness of the 3YSZ electrolyte to be between 1,75 and 2 MPa $\text{m}^{1/2}$ at $T = 950^\circ\text{C}$ [17] an initial crack has to be between 1 and 2 mm in order to get extended. If the crack is close to the edge but still has two ends as seen in Fig. 4 this length might be roughly up to twice as long, since the stress is distributed over two crack edges. After this sub critical length the stress intensity remains above the toughness being able to extend the crack from one edge to the other. Therefore, thermal stresses can explain the occurrence of the radial fracture, which includes the vast majority of cracks. But in order to do so flaws within the millimetre range have to be introduced into the electrolyte.

(iii) *Residual stresses:* The five individual cell layers exhibit different thermal expansion coefficients, which cause thermal mismatch strains hence residual stresses after sintering and cooling upon room temperature. In order to assess these strains, strips of half cells have been prepared. These strips consist of a 160 μm thick 6ScSZ electrolyte and either the two cathode or anode layers. The dimensions were $95 \times 10 \text{ mm}^2$. The cells were sintered while being constrained to be flat. After sintering the different thermal expansions lead to a curvature of the strip, which was measured using a camera. The curvature is then fitted by a circle to obtain its radius. Although the deflection was above the strip thickness, the sample showed no significant inhomogeneous bending. The single electrolyte remains flat even after annealing at the sinter temperature, thus the curvature can be attributed solely to thermal mismatch. When repeating the measurement of one sample, the method gives results with a reproducibility of $\pm 5\%$. It is not possible to determine

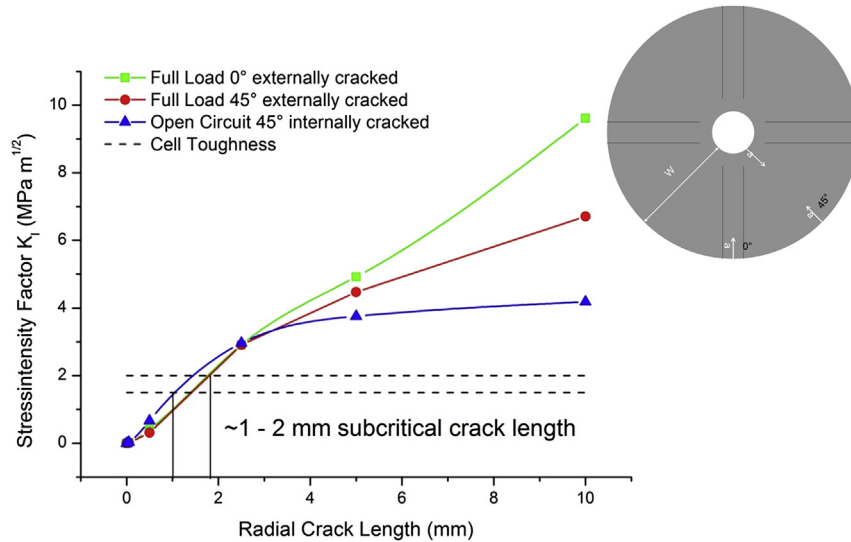


Fig. 9. Stress intensity factor solutions at various angles and internal and external cracks (dots are spline interpolated).

the thermal mismatch strains and thus the residual stresses for all three layers of the half-cell just by measuring the radius of curvature. Therefore, the two electrode layers are considered as one. Compared to the electrolyte the Young's modulus of the electrode layers is similar and their thermal expansion coefficients are close to each other as well. Therefore assuming the electrodes to be one homogeneous layer will not influence the interpretation of the results.

For a bilayer the thermal mismatch strain $\varepsilon_{th} = (\bar{\alpha}_1(\Delta T) - \bar{\alpha}_2(\Delta T))\Delta T$ is easily accessible following the elastic solutions of Hsueh and Evans [22], while applying a thickness weighed average Young's modulus and their combined thickness of the electrode layers. Fig. 10(a) shows the resulting biaxial stress in the electrode and the electrolyte obtained by applying the multi-layer solutions of Hsueh [23]. Additionally the nominal stresses which are to be expected according to the thermal expansion coefficients are presented. For comparison the radius of curvature for strips is calculated using the approach in Refs. [23], the data given in Table 1 and a ΔT which is the difference between RT and the respective sintering temperature. The stresses are then calculated

as for the measured samples taking the two electrode layers as one. The residual stress for a cathode half-cell is relatively small and is close to what could be expected from the expansion mismatch. The deviation might be due to a lower effective temperature difference to the reference temperature (temperature with no residual stress) which is usually lower than the sintering temperature. The surface of the cathode after sintering shows a bubble-like morphology and small separate cracks which are characteristic for the cathode current collecting layer (see Fig. 10(c)). After etching and hence the removal of the LSM from the cathode the residual ceramic 8YSZ backbone of the former cermet structure of the functional cathode layer shows almost no defects.

The opposite is the case for the anode. After sintering the anode exhibits a completely developed channel crack network (see Fig. 10(b)). These channel cracks explain the large deviation from the measured stress and the nominal one, which is almost five times higher. That means that the anode cannot withstand the tension which emerges during cooling after the sintering. After being reduced the anode continues shrinking leading to a slightly increased stress level but leaving the crack pattern unchanged. The

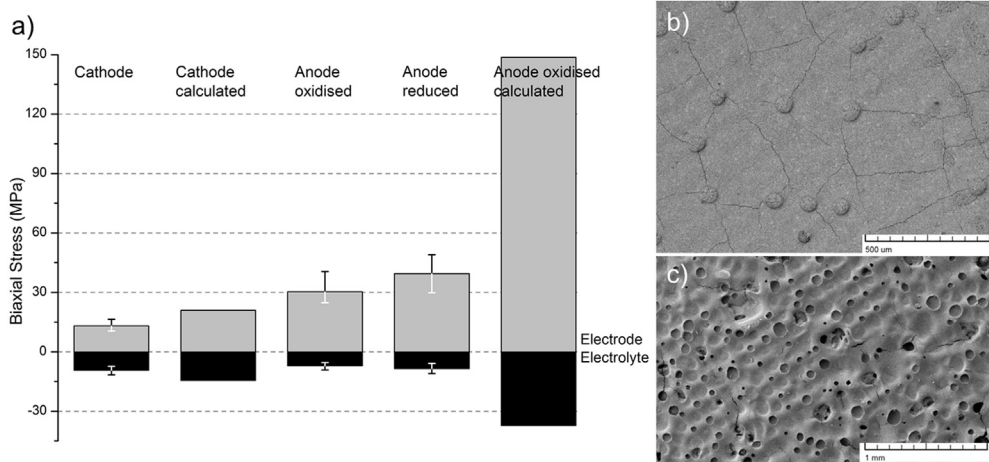


Fig. 10. (a) Residual stresses of cathode and anode half cells at RT from curvature measurements (error bars represent the sample spread) and the corresponding expected stresses based on the thermal expansion coefficients and according to values in Table 1; (b) image of the anode and (c) the cathode surface (BSE detector, 20 kV). The bubbles visible at the surfaces of the two electrode images are a consequence of the manufacturing process.

nominal compressive stress for the electrolyte at RT as part of a whole cell would be almost the sum of the single contributions of the electrodes being $\sigma_{El,nom} = -43$ MPa, while the measured stress would be $\sigma_{El,exp} = -15$ MPa. The residual stress reaches its maximum at RT while it almost vanishes at operation temperature. This becomes even more apparent when taking into account that the reference temperature is always somewhat lower than the sinter temperature and that the reference wanders towards the operating temperature due to creep.

3. Discussion

Fractography reveals that the cell fracture happens in two steps. This is indicated by the two different morphologies of the fracture surface, which are clearly separated by distinct edges curved towards the anode (see Fig. 11). At these edges the crack front comes to a halt. This is supported by the repeated observation of two of these pre-cracks in one extended crack. Underlining that the moment for the pre-crack formation is different from the one when the crack is being extended, otherwise there would be no chance for the development of a second pre-crack. It is obvious that the load which causes the pre-crack initiation is of local nature, while the cause for the overall crack extension has to be global. As already mentioned in Section 2.2, thermal stresses are fulfilling this requirement, as they are able to extend flaws in the range of several millimetres throughout the cell. This leads to the conclusion that the pre-crack has to form when the thermal stresses are absent or less pronounced. This is further supported by the fact that even a combination of the thermal stress peaks and the stresses introduced by the bumps on the cathode side are not sufficient to be the single cause for fracture, since the failure probabilities do not match with the observed damage, especially for the 3YSZ electrolyte (see Fig. 7).

So far only the stresses at the electrolyte have been considered as causes for fracture. But it has been already shown that the strength of the electrolyte can be affected by the electrodes as well [9,10]. Given a substrate which is coated with a more compliant layer, cracks in the layer reaching down to the interface may penetrate into the substrate until a certain depth following laterally the cracks of the coating. This is the case for the anode layers as seen in Fig. 10. The elastic problem of coatings on relatively thick substrates being under residual stress due to thermal mismatch has been already developed by Ye and Suo [24] and reviewed by Hutchinson and Suo [25]. Depending on the elastic constants and the in plane stress and the thickness of the film, an expanding crack in the substrate being nucleated underneath a channel crack would have a positive energy release rate. The rate decreases with the depth. The substrates toughness decides whether a crack propagates and how deep, but in any case the crack extension would be stable.

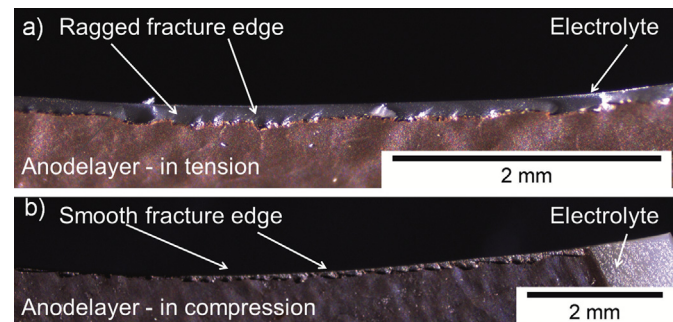


Fig. 12. Fracture edges of an anode half-cell with a 6ScSZ electrolyte after being flexed with the anode being either (a) in tension or (b) under compression.

The situation for the electrolyte as part of the cell is somewhat different as described in Ref. [25]. Because of its comparable thickness with respect to the electrodes it gets significantly compressed when the electrodes are under tension. Therefore the energy release rate for a substrate crack in the electrolyte is lowered if not negative. Hence it is no surprise that without an external mechanical load no damage to the electrolyte due to the highly stressed anode is observed. Nonetheless, if an external load is applied to the cell overcoming the compressive stress and increasing the overall energy release rate for an into the substrate expanding channel crack, the anode will then become the strength determining element of the cell. Fig. 12 is a comparison between the fracture surfaces of an anode half-cell (electrolyte with only one electrode) with a 6ScSZ electrolyte flexed either with the anode side or the uncoated electrolyte side under tension. In the first case the morphology is jagged as for the pre-cracks in the actual ruptured cells (compare Fig. 4). In the second case, the electrolyte surface is smooth while the anode still displays a zigzag fracture line. The reason for this distinct behaviour of the anode is the fact that it is already greatly damaged, so that a global crack will follow the pre-existing channel cracks. If tension is applied on the anode, these cracks will be able to penetrate into the electrolyte imprinting the fracture path of the anode in the electrolyte. By comparing the morphology of Fig. 12(a) and 4 it becomes apparent that the crack origins for the observed pre-cracks are the pre-existing channel cracks of the anode. The driving force for the propagation of these cracks into the electrolyte is given in any case by the inhomogeneous MIC-Cell contact (in the form of the bumps, the contact coating or the disintegration of the cathode at the fuel sealing plane) leading to multiple local stress peaks in the cell and the residual stress in the anode due to thermal mismatch. Both of these driving forces increase with decreasing temperature competing against the rising fracture toughness of the electrolyte, which gives a hint that the pre-cracks are formed during the cooling or the heating up of the stack. Additionally the electrolyte might exhibit a so called low thermal degradation (LTD). This is a phenomena

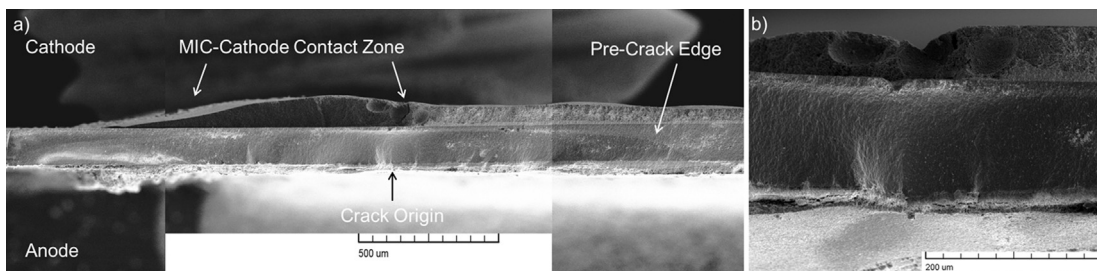


Fig. 11. (a) Pre-crack zone of a cell fractured at sealing plane at the air inlet; (b) Crack origin.

characteristic to tetragonal stabilized zirconia like 3YSZ and 6ScSZ, where the strength severely suffers if the material is exposed to a humid media at temperatures between 150 and 400 °C [26]. During cooling the stack needs several hours in order to reach RT, while residual moisture might linger in the fine pore structure of the functional anode layer. Furthermore, the Nickel of the anode undergoes a magnetic phase transition between 200 and 300 °C so that the thermal expansion coefficient rises relatively steeply coming from high temperatures until it reaches a maximum at 240 °C [27]. Hence, the residual stress will rise accordingly. LTD and this non-monotonic behaviour of thermal mismatch strain might crucially affect the failure probability and the formation of pre-cracks.

The explanation as for why the fracture origins for widely extended cracks are correlated with the stress peaks for the two presented operating conditions can now be given. Pre-cracks are probably formed throughout the whole cell since bumps on the cathode side are found for arbitrary sites at the MIC. The probability for these pre-cracks to propagate depends on the local thermal stress level, thus the stress peaks in Fig. 8 correspond with red areas marking frequent sites for crack origins, it is there that the probability for a pre-crack to get “picked up” is greatest.

In order to prove these hypotheses it is necessary to measure the bi-axial bending strength of the cell over the whole temperature range in its oxidised state and for the operating temperature in its reduced one. Because the loads present are deformation controlled the critical strain of the electrolyte and the critical deflection of the whole cell should be taken into account in order to assess the susceptibility of the cell for fracture within the stack.

Furthermore, it remains unclear how the microstructural changes within the anode during operation, which have been reported by Holzer et al. for this anode material [28,29], will affect the residual stresses. Additionally, for most of the Ni-based anode materials significant creep rates are to be expected at operating temperature [30]. Since all discussed sources for stress are deformation controlled, creep would simply relax crucial stresses and it would be therefore beneficial. However, the creep rate is mostly determined by the ceramic backbone which is with CGO different from the so far reported zirconia based ones. Hence, it is at this point not possible to consider possible creep effects.

4. Conclusion

Nine SOFC stacks of the Galileo 1000 N being operated at customers sites or at Hexis have been inspected post mortem. Each examined stack contained fractured cells. After a fractographical and fracture mechanical analysis it becomes apparent that for almost all of the cells fracture happens according to one distinct failure pattern. When mounted, the anode of the cell exhibits channel cracks as a consequence of the large thermal mismatch to the electrolyte. Due to the occurrence of bumps on the cathode side and the disintegration of the cathode at the fuel sealing around the central hole, the pre-load leads to local stress peaks loading predominantly the anode side of the cell. Along with residual stresses in the anode either due to thermal mismatch or the shrinkage due to the Ni-reduction, the anode's channel cracks are able to propagate into the electrolyte. Because the external stress for the cell is local and deformation controlled, a stable pre-crack forms in the electrolyte most likely when the stack is below the operating temperature, hence while it is either cooling down, heating up or

idle at RT. Such a damaged cell will most likely rupture at places where thermal stresses are high. These sites are at the air entrance while the stack operates at MPO-conditions and around the central hole in the case of an OC. Pre-cracks might form in the whole cell but appear to be critical mostly at these areas.

Based on this failure analysis it is now possible to evaluate general and system specific design guidelines in order to reduce the cells failure probability, which will be part of a subsequent study.

Acknowledgements

The authors would like to thank R. Bächtold, U. Weissen, B. Iwanschitz, D. Haberstock, R. Denzler and J.A. Schuler for the priceless discussions and the unconditional support. Furthermore, the funding of this work by the Swiss Federal Office of Energy under the contract no. 8100076; SI/500084-02 and by Swissselectric Research within the SOF-CH-ESC project is gratefully acknowledged.

References

- [1] M.Y. Gong, X.B. Liu, J. Trembly, C. Johnson, *J. Power Sources* 168 (2007) 289–298.
- [2] N. Shaigan, W. Qu, D.G. Ivey, W.X. Chen, *J. Power Sources* 195 (2010) 1529–1542.
- [3] M. Ettler, H. Timmermann, J. Malzbender, A. Weber, N.H. Menzler, *J. Power Sources* 195 (2010) 5452–5467.
- [4] H. Yokokawa, H. Tu, B. Iwanschitz, A. Mai, *J. Power Sources* 182 (2008) 400–412.
- [5] J. Malzbender, P. Batfalsky, R. Vaßen, V. Shemet, F. Tietz, *J. Power Sources* 201 (2012) 196–203.
- [6] J. Laurencin, G. Delette, F. Lefebvre-Joud, A. Dupeux, *J. Eur. Ceram. Soc.* 28 (2008) 1857–1869.
- [7] A. Atkinson, A. Selcuk, *Acta Mater.* 47 (1999) 867–874.
- [8] J. Malzbender, R.W. Steinbrech, *J. Eur. Ceram. Soc.* 27 (2007) 2597–2603.
- [9] A. Selcuk, A. Merere, A. Atkinson, *J. Mater. Sci.* 36 (2001) 1173–1182.
- [10] B.F. Sorensen, S. Prindahl, *J. Mater. Sci.* 33 (1998) 5291–5300.
- [11] A. Mai, B. Iwanschitz, U. Weissen, R. Denzler, D. Haberstock, V. Nerlich, A. Schuler, in: S.C. Singhal, K. Eguchi (Eds.), *Solid Oxide Fuel Cells*, 12, 2011, pp. 87–95.
- [12] A. Hessler-Wyser, Z. Wuillemin, J.A. Schuler, A. Faes, J. Van Herle, *J. Mater. Sci.* 46 (2011) 4532–4539.
- [13] M. Chen, Y.L. Liu, A. Hagen, P.V. Hendriksen, F.W. Poulsen, *Fuel Cells* 9 (2009) 833–840.
- [14] W.C. Young, R.G. Budynas, *Roark's Formulas for Stress and Strain*, seventh ed., MacGraw-Hill, New York, 2002.
- [15] C.H. Hsueh, C.R. Luttrell, *Compos. Sci. Technol.* 67 (2007) 278–285.
- [16] R. Danzer, T. Lube, P. Supancic, R. Damani, *Adv. Eng. Mater.* 10 (2008) 275–298.
- [17] J. Kuebler, U.F. Vogt, D. Haberstock, J. Sfeir, A. Mai, T. Hocker, M. Roos, U. Harnisch, *Fuel Cells* 10 (2010) 1066–1073.
- [18] M. Roos, E. Batawi, U. Harnisch, T. Hocker, *J. Power Sources* 118 (2003) 86–95.
- [19] D. Munz, T. Fett, *Ceramics*, first ed., Springer, Berlin, 2001.
- [20] G.A. Schneider, R. Danzer, *Eng. Fract. Mech.* 34 (1989) 547–552.
- [21] X.R. Wu, A.J. Carlsson, *Weight Functions and Stress Intensity Factor Solutions*, first ed., Pergamon Press, Oxford, 1991.
- [22] C.H. Hsueh, A.G. Evans, *J. Am. Ceram. Soc.* 68 (1985) 241–248.
- [23] C.H. Hsueh, *Thin Solid Films* 418 (2002) 182–188.
- [24] T. Ye, Z. Suo, A.G. Evans, *Int. J. Solids Struct.* 29 (1992) 2639–2648.
- [25] J.W. Hutchinson, Z. Suo, *Adv. Appl. Mech.* 29 (1992) 63–191.
- [26] J. Chevalier, L. Gremillard, A.V. Virkar, D.R. Clarke, *J. Am. Ceram. Soc.* 92 (2009) 1901–1920.
- [27] M. Mori, T. Yamamoto, H. Itoh, H. Inaba, H. Tagawa, *J. Electrochem. Soc.* 145 (1998) 1374.
- [28] L. Holzer, B. Iwanschitz, T. Hocker, B. Münch, M. Prestat, D. Wiedenmann, U. Vogt, P. Holtappels, J. Sfeir, A. Mai, T. Graule, *J. Power Sources* 196 (2011) 1279–1294.
- [29] L. Holzer, B. Münch, B. Iwanschitz, M. Cantoni, T. Hocker, T. Graule, *J. Power Sources* 196 (2011) 7076–7089.
- [30] A. Nakajo, J. Kuebler, A. Faes, U.F. Vogt, H.J. Schindler, L.-K. Chiang, S. Modena, J. Van Herle, T. Hocker, *Ceram. Int.* 38 (2012) 3907–3927.